Journal of Materials Chemistry A

ROYAL SOCIETY OF CHEMISTRY

PAPER

View Article Online
View Journal | View Issue

Cite this: J. Mater. Chem. A, 2025, 13, 39426

Z-Scheme heterojunction formation between $CsPbBr_3$ and BiOBr: key to singlet oxygen formation for selective semidehydrogenation of tetrahydroisoquinoline

Vishesh Kumar,[a] Sunil Kumar Patel,[b] Shivali Dhingra,[c] Deepak Kumar,[a] Ved Vyas,[a] Kamalakannan Kailasam,*[c] E. Siva Subramaniam Iyer*[b] and Arindam Indra*[a]

Received 7th June 2025
Accepted 12th October 2025

DOI: 10.1039/d5ta04618a

rsc.li/materials-a

Herein, a Z-scheme heterojunction has been constructed using BiOBr nanosheets (NSs) and $CsPbBr_3$ quantum dots (QDs) for the selective semidehydrogenation of 1,2,3,4-tetrahydroisoquinoline (THIQ) to 3,4-dihydroisoquinoline (DHIQ). The interfacial internal electric field directs the photogenerated electron transfer from the conduction band (CB) of BiOBr to the valence band (VB) of $CsPbBr_3$, resulting in an effective separation and transport of photogenerated charges. Furthermore, the heterojunction photocatalyst facilitates the activation of triplet oxygen to singlet oxygen. The optimized amount of $CsPbBr_3$ QDs (20 wt%) loaded on BiOBr NSs (Z-20) achieved 97% yield of DHIQ by the selective semidehydrogenation process. The appropriate band alignment in Z-20 ensures two-electron selectivity for the semidehydrogenation of THIQ in contrast to other heterojunctions, constructed by the combination of different photocatalysts. Transient absorption spectroscopy reveals optimized exciton behavior in Z-20, characterized by fast internal relaxation and trapping, which affects the catalytic efficiency.

Introduction

Semiconductor-based heterostructures show optimal optical properties, controllable bandgaps, and modulated optoelectronic properties, offering wide applications in light-emitting diodes, solar cells, photocatalytic energy conversion processes, organic pollutant degradation, and organic transformation reactions.[1–3] The heterojunction formation effectively separates photogenerated electrons and holes while combining the benefits of each component.[4–8] Among these, Z-scheme heterojunctions, composed of oxidation and reduction photocatalysts, are the most promising because of the advantages such as: (i) suppression of charge recombination, (ii) availability of reducing electrons and oxidizing holes, (iii) improved light absorption, and (iv) tuning of the lifetime of the charge carriers.[9] Z-Scheme photocatalysts have been successfully employed for the photocatalytic H_2 evolution, CO_2 reduction, N_2 reduction, and organic transformation reactions.[10–13]

In this study, we have demonstrated the formation of a Z-scheme heterojunction of bismuth oxybromide (BiOBr) nanosheets (NSs) and metal halide perovskite $CsPbBr_3$ quantum dots (QDs) and its application for the semidehydrogenation of 1,2,3,4-tetrahydroisoquinoline (THIQ) in the presence of $^3O_2$ as the green electron acceptor (Fig. 1). Recently, BiOBr nanoparticles have gained significant attention for their outstanding visible-light photocatalytic activity, enabled by their unique

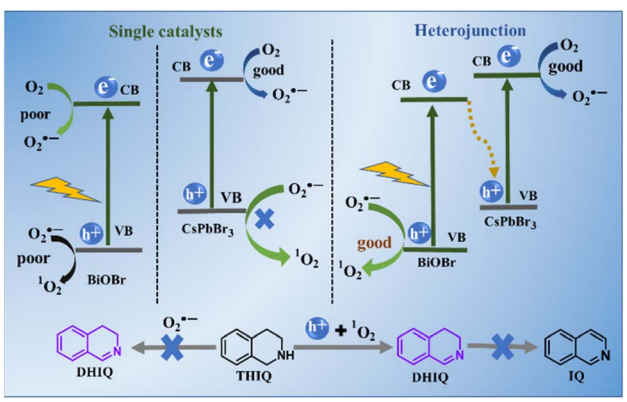

Fig. 1 Schematic representation of molecular oxygen activation and hole utilization with the $CsPbBr_3$/BiOBr heterojunction photocatalyst (Z-20) for the semidehydrogenation of 1,2,3,4-tetrahydroisoquinoline.

[a]Department of Chemistry, Indian Institute of Technology (BHU), Varanasi-221005, UP, India. E-mail: arindam.chy@iitbhu.ac.in

[b]School of Chemical and Materials Sciences, Indian Institute of Technology Goa, Ponda, Goa, India. E-mail: essiyer@iitgoa.ac.in

[c]Advanced Functional Nanomaterials, Institute of Nano Science and Technology (INST), Knowledge City, Sector-81, Manauli, SAS Nagar, 140306 Mohali, Punjab, India. E-mail: kamal@inst.ac.in

layered structure that promotes efficient charge separation and enhanced photoactivity.[14,15] Additionally, the valence band maximum (VBM) of BiOBr is positive enough to convert $O_2^{\bullet-}$ to $^1O_2$. However, BiOBr showed poor activity for the activation of $^3O_2$ to $O_2^{\bullet-}$ in the presence of light (Fig. 1).[16]

In contrast, $CsPbBr_3$ possesses a sufficiently negative conduction band minimum (CBM), suitable for the single electron reduction of $^3O_2$ to $O_2^{\bullet-}$.[17–19] Therefore, the Z-scheme heterojunction of $CsPbBr_3$/BiOBr can activate $^3O_2$ from air to form $O_2^{\bullet-}$ and subsequently $^1O_2$, which can be effectively utilized for organic transformation reactions. In addition, $CsPbBr_3$ is known for its optoelectronic properties, including a large extinction coefficient, high light absorption properties, and high charge carrier mobility.[20] The inherent soft crystal lattice of $CsPbBr_3$ also allows high tolerance to lattice mismatch, revealing new opportunities for heterojunction formation with other semiconductors.[21]

In this study, we have explored the photocatalytic selective semidehydrogenation of THIQ to DHIQ using Z-scheme catalysts. DHIQ is a valuable intermediate in the drug and pharmaceutical industries, and it can be synthesized by the semidehydrogenation of THIQ.[22] Recently, electrocatalytic approaches have been introduced for the selective $2e^-$ oxidation of THIQ using different transition metal-based catalysts.[23,24] In contrast, photocatalytic semidehydrogenation of THIQ to DHIQ is rarely studied. The process is highly challenging because of the need for control over the number of electron and proton transfers ($2e^-/2H^+$ *vs.* $4e^-/4H^+$). Also, the semidehydrogenation of THIQ is more difficult as the complete dehydrogenation results in the favorable aromatization to isoquinoline (IQ) (Fig. 1).[25–27]

Recently, the Wang group reported photocatalytic dehydrogenation of THIQ with h-BCN but ended up with the formation of IQ.[28] Furthermore, the Bahnemann group reported Rh/TiO_2-photocatalyzed dehydrogenation of THIQ, yielding a mixture of DHIQ and IQ.[26] These studies highlight that the semidehydrogenation of THIQ to DHIQ remains a highly challenging process. However, the Shi group successfully utilized $Zn_3In_2S_6$ for the photocatalytic semidehydrogenation of THIQ using molecular $^3O_2$ as the electron acceptor.[29] In further advancement, the Li group demonstrated semidehydrogenation of THIQ using a $MoS_2/ZnIn_2S_4$ heterojunction.[30]

The success of the above studies led us to design Z-scheme heterojunctions of *x*%-$CsPbBr_3$/BiOBr (*viz.* Z-*x*, $x = 10$, 20, and 30 weight%) for the controlled semidehydrogenation of THIQ in the presence of $^3O_2$ as the green electron acceptor. The Z-scheme heterojunction fine-tunes the band positions to form $O_2^{\bullet-}$ and $^1O_2$ by the activation of $^3O_2$ and facilitates the hydrogen abstraction process.[22] Although $CsPbBr_3$ can produce $O_2^{\bullet-}$, the formation of DHIQ by semidehydrogenation of THIQ was negligible. In contrast, BiOBr produced a moderate yield (56%) of DHIQ, while Z-20 showed a high yield of 97%. The formation of $^1O_2$ was found to be crucial to control the selectivity for the semidehydrogenated product DHIQ.

The formation of Z-scheme heterojunctions was confirmed by various spectroscopic methods. Furthermore, improved charge separation, transport, and suppression of the recombination of photogenerated charge carriers were proved by electrochemical impedance spectroscopy (EIS), photocurrent measurements, and photoluminescence studies. Femtosecond transient absorption spectroscopy (fs-TAS) reveals a faster relaxation rate in Z-20 than in $CsPbBr_3$, indicating the acceleration of the exciton relaxation in the heterojunction due to the carrier trapping on a short time scale.

Results and discussion

Synthesis and characterization of heterojunction catalysts

BiOBr NSs were synthesized by the solvothermal method, whereas $CsPbBr_3$ QDs were prepared by the hot injection method.[21,31,32] Furthermore, Z-10, Z-20, and Z-30 heterojunctions were prepared by the physical mixing of different weight% (10, 20, and 30) of $CsPbBr_3$ QDs with BiOBr NSs (Table S1). Although all the heterojunction catalysts showed improved charge transport and $^3O_2$ activation compared to the single photocatalysts, the appropriate amount (20%) of loading of $CsPbBr_3$ on BiOBr produced the maximum photoactivity (see later). Therefore, extensive characterization was performed for Z-20 and compared to those of bare BiOBr and $CsPbBr_3$.

Powder X-ray diffraction (PXRD) of Z-20 confirmed all the characteristic diffractions from $CsPbBr_3$ (cubic phase, space group = $Pm\bar{3}m$, JCPDS no. 54-0752) and BiOBr (tetragonal phase, space group = $P4/nm$, JCPDS no. 73-2061) (Fig. S1).[21,32] PXRD also indicates that $CsPbBr_3$ QDs are deposited on the (001) facet of BiOBr NSs as the intensity of the (001) peak decreases in Z-20 compared to pure BiOBr (Fig. S1).

Transmission electron microscopy (TEM) revealed an average particle size of 8 ± 2 nm for $CsPbBr_3$ QDs (Fig. 2a). High-resolution TEM (HR-TEM) confirmed the formation of a heterojunction between $CsPbBr_3$ and BiOBr (Fig. 2b). The lattice spacing of 0.27 nm was observed for the (110) facet of BiOBr (rectangle) and 0.413 nm for the (110) facet of $CsPbBr_3$ (circle) (Fig. 2c and d).[21,32] Fast Fourier transform (FFT) and inverse FFT analyses revealed the lattice spacing corresponding to 0.41 nm and 0.27 nm for $CsPbBr_3$ and BiOBr, respectively (Fig. 2c′, d′ and c″, d″). Additionally, the energy-dispersive X-ray (EDX) spectra of $CsPbBr_3$, BiOBr, and Z-20 confirmed the presence of corresponding elements (Fig. S2). EDX elemental mapping of Z-20 also showed a uniform distribution of the elements (Fig. 2e–i and S3).

X-ray photoelectron spectroscopy (XPS) was carried out to understand the electronic interaction between BiOBr and $CsPbBr_3$ in Z-20 (Fig. 2j–l).[21,32] The binding energies (BEs) of Cs 3d, Pb 4f, and Br 3d in Z-20 are positively shifted compared to those of pristine $CsPbBr_3$, indicating the electron-deficient nature of the elements in $CsPbBr_3$ after the integration with BiOBr (Fig. 2j, k and S4). In contrast, Bi in Z-20 turns into more electron-rich (negative shift in the BEs of Bi 4f in Z-20) compared to that in BiOBr to balance the electron redistribution in Z-20 (Fig. 2l). These results implied electron transfer from $CsPbBr_3$ to BiOBr after contact because of their different energy band potentials, generating an internal electric field (IEF), directed from $CsPbBr_3$ to BiOBr in the absence of light. The generation of the IEF facilitates the charge separation in Z-

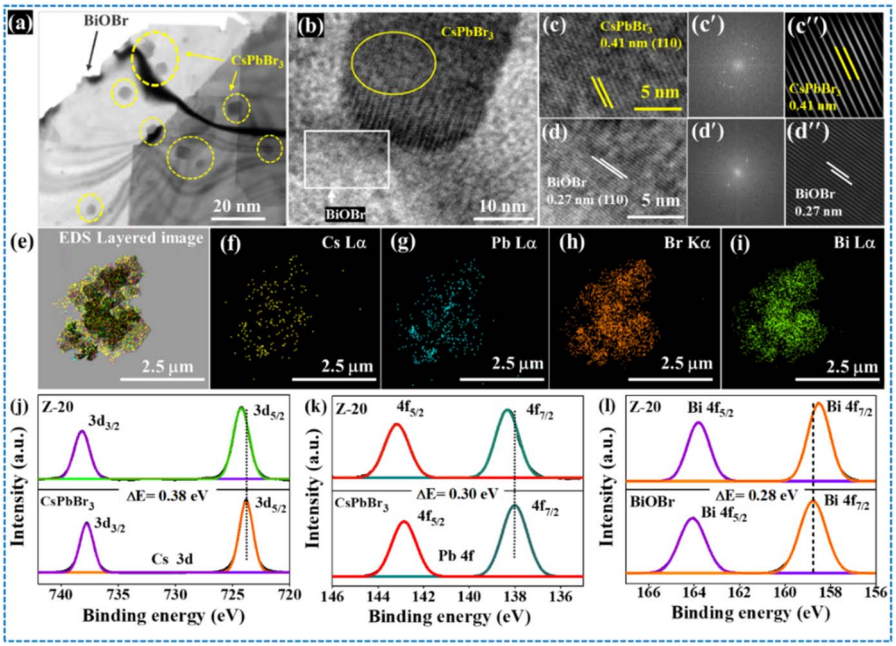

Fig. 2 (a) TEM image of Z-20 showing the deposition of $CsPbBr_3$ QDs on the surface of BiOBr nanosheets. $CsPbBr_3$ QDs on the surface of BiOBr are marked with circles. (b) HR-TEM confirmed the formation of a heterojunction between QDs and BiOBr. (c and d) Lattice spacings of 0.41 nm for $CsPbBr_3$ QDs and 0.27 nm for BiOBr, corresponding to the (110) planes of both semiconductors. (c′ and d′) Selected area FFT showing the diffractions for $CsPbBr_3$ and BiOBr in Z-20. (c″ and d″) Inverse FFT of figures (c′) and (d′), respectively. (e–i) EDX elemental mapping of Z-20. (j) Cs 3d XP spectra of $CsPbBr_3$ QDs and Z-20; (k) Pb 4f XP spectra of $CsPbBr_3$ QDs and Z-20; and (l) Bi 4f XP spectra of BiOBr and Z-20.

20 and improves the photocatalytic semidehydrogenation of THIQ. The Br 3d and O 1s XPS spectra of $CsPbBr_3$, Z-20, and BiOBr are shown in Fig. S4.

Z-Scheme *vs.* type-II heterojunction

Ultraviolet-visible diffuse reflectance spectroscopy (UV-DRS) studies were carried out to understand the light absorption properties of $CsPbBr_3$, BiOBr, and Z-scheme photocatalysts (Z-10, Z-20, and Z-30) (Fig. 3a and S5a).[21,32] $CsPbBr_3$ and BiOBr showed absorption edge at 534 nm and 445 nm, respectively. The heterojunction Z-20 exhibited absorption behavior between that of $CsPbBr_3$ and BiOBr, indicating strong electronic interactions. The Tauc plot calculated the bandgaps as 2.32 eV for $CsPbBr_3$ and 2.77 eV for BiOBr NSs. Interestingly, the bandgap of $CsPbBr_3$ remained unchanged after being loaded on the surface of BiOBr, attributed to the strong absorption properties of $CsPbBr_3$ (Fig. 3a inset and S5b).

Mott–Schottky (MS) plots showed the formation of an n–n-heterojunction between $CsPbBr_3$ and BiOBr (Fig. 3b and c).[32] The flat band potential (E_{fb}) of $CsPbBr_3$ was calculated to be −0.92 eV *vs.* the normal hydrogen electrode (NHE), and similarly, the E_{fb} of BiOBr was determined to be −0.56 eV *vs.* NHE, and the E_{CB} values for $CsPbBr_3$ and BiOBr were determined to be −1.02 eV and −0.66 eV *vs.* NHE, respectively. Therefore, the valence band maximum potentials (E_{VB}) of $CsPbBr_3$ and BiOBr were calculated to be 1.30 eV *vs.* NHE and 2.11 eV *vs.* NHE, respectively.

Furthermore, valence band XPS analyses were conducted to determine the energy difference between the VBM and the Fermi level (E_F) of the catalysts.[2,3] The E_F–E_{VB} values were found to be 1.28 eV for $CsPbBr_3$ and 1.93 eV for BiOBr (Fig. 3d and e). Based on these data, the band alignments in $CsPbBr_3$, BiOBr, and Z-20 are shown in Fig. 3f. The staggered alignment of energy bands between $CsPbBr_3$ and BiOBr is crucial for the formation of a Z-scheme/type-II heterojunction (Fig. 4). As the E_F position of BiOBr is notably lower than that of $CsPbBr_3$, the formation of a Z-scheme heterojunction is favorable in the presence of light. When the heterojunction is irradiated with light, the transfer of photogenerated electrons from the CB of BiOBr to the VB of $CsPbBr_3$ forms a Z-scheme and facilitates the separation of holes and electrons. Further evidence for the Z-scheme formation is detailed in the next section.

Z-Scheme heterojunction

The work function (Φ) calculations (Φ_{CsPbBr_3}: 4.20 eV and Φ_{BiOBr}: 6.01 eV) from ultra-violet photoelectron spectroscopy (UPS) confirmed the surface potential flow from BiOBr to $CsPbBr_3$ in Z-20 (Fig. S6). The larger work function of BiOBr indicates a lower E_F than that of $CsPbBr_3$.[33–35] Therefore, spontaneous electron transfer from $CsPbBr_3$ to BiOBr takes place in close contact (in the dark) until their Fermi levels at the interface are aligned. This generates an electron depletion layer in $CsPbBr_3$ and an electron accumulation layer in BiOBr. At the interface, $CsPbBr_3$ becomes positively charged and BiOBr is negatively charged, leading to an energy band bending and a built-in electric field directed from $CsPbBr_3$ to BiOBr (Fig. 4a). These phenomena promote the photoinduced electron transfer from the E_{CB} of BiOBr across the interface to combine with

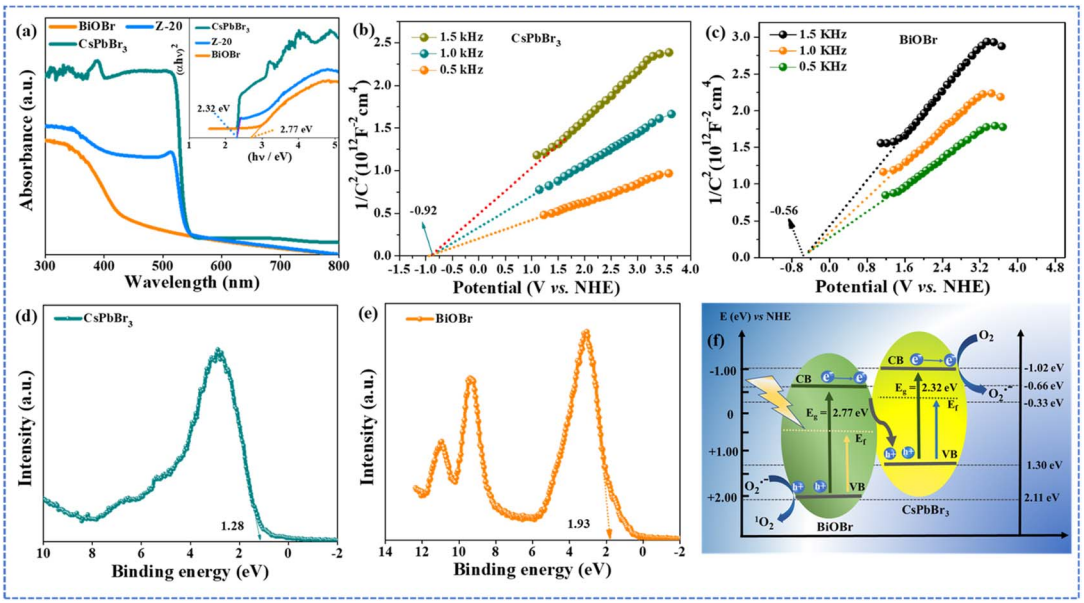

Fig. 3 (a) UV-vis diffuse reflectance spectra of $CsPbBr_3$ QDs, Z-20, and BiOBr, with the inset showing the corresponding Tauc plot, demonstrating no significant change in the bandgap of $CsPbBr_3$ after the introduction of $CsPbBr_3$ QDs to BiOBr nanosheets. (b and c) Mott–Schottky plots of (b) $CsPbBr_3$ and (c) BiOBr. (d and e) Valence band XPS spectra of (d) $CsPbBr_3$ and (e) BiOBr. (f) Depiction of the conduction band minima and valence band maxima for $CsPbBr_3$ QDs and BiOBr NSs, derived from the Tauc plot and Mott–Schottky studies. Note: photoelectrochemical measurements were conducted under neutral conditions (pH = 7).

photoinduced holes of $CsPbBr_3$, confirming a Z-scheme electron transfer. The Z-scheme formation improved the charge carrier separation with higher availability of holes in the VB of BiOBr and electrons in the CB of $CsPbBr_3$.

To further study the charge transfer mechanism in Z-20, EPR analysis was conducted (see the details of the experiments in the SI). The radical trapping agent 5,5-dimethyl-1-pyrroline-*N*-oxide (DMPO) was used to capture photogenerated reactive oxygen species, such as $O_2^{\bullet-}$ radicals (Fig. 4b and c).[2] Under simulated sunlight, DMPO–$O_2^{\bullet-}$ signals with four characteristic peaks were observed for Z-20. However, the peak intensity ratio was not found to be 1 : 1 : 1 : 1 because of the presence of multiple reactive oxygen species, including $O_2^{\bullet-}$ and $^1O_2$ in the reaction medium (Fig. 4b).[36] This observation is consistent with earlier studies where overlapping signals and secondary reactions of $O_2^{\bullet-}$ hinder the appearance of well-resolved

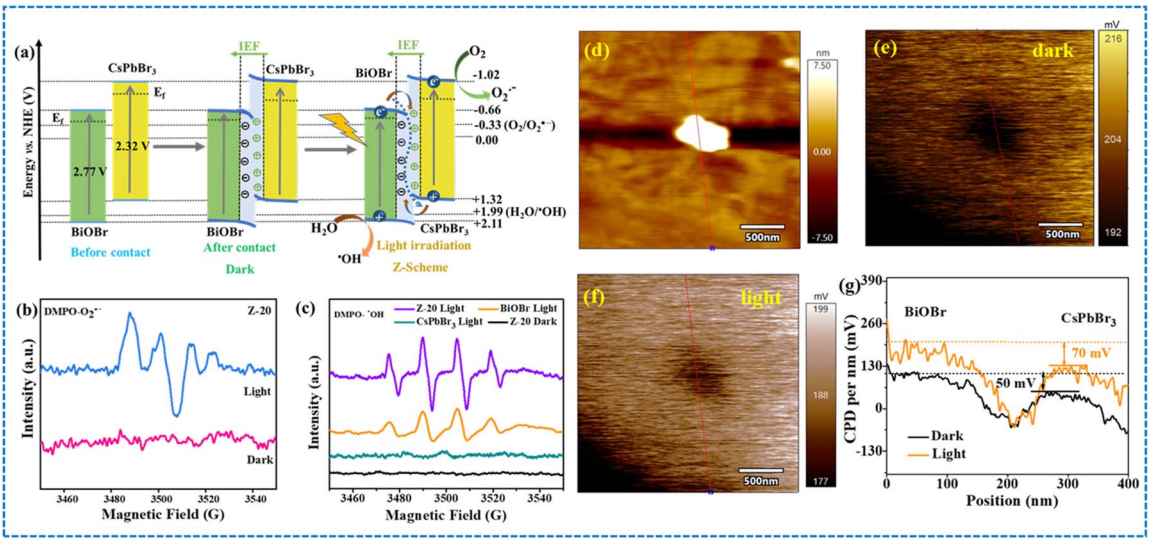

Fig. 4 (a) Schematic representation of the BiOBr/$CsPbBr_3$ heterojunction: internal electric field (IEF) induced charge transfer, separation, and Z-scheme heterojunction formation under UV-visible light irradiation for photocatalytic semidehydrogenation of THIQ. (b) EPR spectra of DMPO–$O_2^{\bullet-}$ and (c) DMPO–$^{\bullet}$OH. (d–g) Comparative KPFM study of $CsPbBr_3$/BiOBr: (d) AFM height image, (e) surface potential images in the dark, (f) under light, and (g) the corresponding profiles of contact potential difference (CPD) per nm *vs.* position.

characteristic peaks (Fig. 4b).[3,37] As the E_{CB} of Z-20 is sufficiently negative to reduce O_2, the stronger DMPO–$O_2^{\bullet-}$ signals for Z-20 suggest a higher number of photoexcited electrons accumulated in the CB of $CsPbBr_3$.

To confirm the formation of a Z-scheme and not a type-II heterojunction, we have introduced H_2O in the reaction mixture. The formation of $^{\bullet}OH$ radicals confirms the Z-scheme heterojunction between $CsPbBr_3$ and BiOBr, as the type-II heterojunction cannot produce $^{\bullet}OH$ radicals because the VB potential is not high enough for the oxidation of H_2O to $^{\bullet}OH$ radicals (Fig. S7).

In the EPR spectra, BiOBr and Z-20 showed four characteristic peaks (1 : 2 : 2 : 1) of DMPO–$^{\bullet}OH$ adducts (Fig. 4c).[2] However, the VB potential of bare $CsPbBr_3$ is not high enough to form $^{\bullet}OH$ radicals, and hence no DMPO–$^{\bullet}OH$ adduct was detected in the EPR.[38–40] In addition, $^{\bullet}OH$ radicals were detected in the presence of Z-20 by photoluminescence study using the terephthalic acid–$^{\bullet}OH$ adduct as the probe (peak at 440 nm) (Fig. S8).[37] These findings strongly support that the charge transfer in the Z-20 system follows a Z-scheme mechanism rather than a type-II process.

To further confirm the spatial charge separation of the photo-generated charges by the Z-scheme mechanism, photo-assisted Kelvin probe force microscopy (KPFM) was conducted, and surface potential distribution was determined on the $CsPbBr_3$/BiOBr heterostructure (Fig. 4d–g).[41,42] A representative interfacial region was selected to monitor changes in surface potential before and after illumination with light. In the dark, the surface potential of $CsPbBr_3$ was $\approx$50 mV lower than that of BiOBr. After light illumination, the local surface potential shifted, and the potential difference between $CsPbBr_3$ and BiOBr increased to $\approx$70 mV. This change indicates the accumulation of photogenerated electrons on the surface of $CsPbBr_3$, which is consistent with the UPS potential measurements (Fig. S6). Such a pronounced shift in surface potential under illumination provides direct evidence of spatial charge separation through Z-scheme charge transfer in the $CsPbBr_3$/BiOBr heterostructure (Fig. 4a).

Charge transfer dynamics

Photocurrent measurement was performed to elucidate the separation of photogenerated electron–hole pairs (Fig. 5a and S9). Typically, a higher photocurrent density indicates faster charge separation properties of photogenerated electrons and holes.[43] Notably, BiOBr and $CsPbBr_3$ exhibited relatively low current densities, indicating poor charge separation of photo-induced carriers. In contrast, the heterojunction enhanced the photocurrent density, with Z-20 exhibiting a higher photocurrent compared to the individual photocatalysts and other compositions (Z-10 and Z-30) (Fig. 5a and S9). This demonstrates better photogenerated charge carrier separation efficiency in Z-20.

Electrochemical impedance spectroscopy (EIS) revealed the charge transport properties of the photocatalysts. Z-20 showed the lowest charge transfer resistance compared to $CsPbBr_3$ and BiOBr (Fig. 5b and S10).

The strong photoluminescence (PL) peaks for bare BiOBr and $CsPbBr_3$ were observed at 483 and 510 nm, respectively. After the Z-scheme formation, the peak intensity followed the order: Z-30 > Z-10 > Z-20 (Fig. 5c and S11). This decrement in the peak intensities indicates a suppression in the radiative recombination after heterojunction formation.[44] Interestingly, the PL of BiOBr is quenched irrespective of the different loadings of $CsPbBr_3$ on it (Fig. 5c and S11).

Femtosecond transient absorption spectroscopy study

The fs-TAS study was carried out to understand the ultrafast dynamics of exciton recombination behavior in bare $CsPbBr_3$ QDs and the Z-20 heterostructure. The $CsPbBr_3$ QDs were subjected to excitation at 370 nm, above the band edge of $CsPbBr_3$, to generate charge carriers, leading to the formation of the trap states.[45]

The TA spectra of $CsPbBr_3$ exhibited two distinct spectral features (Fig. 5d and S12a): (i) a pronounced photo-induced absorption (PIA), originating from the probe-induced excitation of photoexcited charge carriers, in the blue region (450–515 nm, having a maximum at 505 nm), and (ii) a broad photo-induced bleach (PIB) in the red region of the spectra (520–600 nm, with a maximum of 518 nm). The PIB signals are attributed to the ground state bleach and stimulated emission.[46]

The Z-20 heterojunction was excited at 370 nm, and its TA spectra are shown in Fig. 5e and S12b. PIA and PIB bands are centred at 511 nm and 525 nm, respectively. The characteristic ground state bleaching signal is attributed to state filling by electrons, which is decreased with heterostructure formation in Z-20.

We have studied the kinetic traces at various probe wavelengths to observe the evolution and subsequent relaxation of the trap states (Fig. 5f–i). The kinetics of the aforementioned spectral features were fitted with a sum of exponentials containing a long-lived component and are tabulated in Table S2. The spectral evolution rates of $CsPbBr_3$ QDs and Z-20 differ significantly. The kinetic traces at 490 nm and 500 nm correspond to the PIA (Fig. 5f and g). The 550 nm kinetics correspond to bleach recovery of the ground state from a higher energy state. The PIB band features also match with the UV absorption bands (Fig. 5h and 3a).

The decay traces reveal that a three-step pathway governs the relaxation of photogenerated electrons. $CsPbBr_3$ deposition onto BiOBr leads to faster kinetics in the TA measurements. The kinetic traces monitored at 500 nm show an initial rise of PIA in $CsPbBr_3$ QDs and Z-20. The PIA decays significantly faster in Z-20 than in $CsPbBr_3$ (Fig. 5h). The lifetimes at 500 nm were observed to be 100 $\pm$ 20 ps and 1300 $\pm$ 200 ps for $CsPbBr_3$ and 20 $\pm$ 2 ps and 700 $\pm$ 200 ps for Z-20 (Table S2).[47] The 100 $\pm$ 20 ps lifetime in $CsPbBr_3$, corresponding to the decay of the excited electron, was decreased by an order of magnitude and appeared as 20 $\pm$ 2 ps in Z-20.

In $CsPbBr_3$, the recovery of the bleach at 550 nm was fitted to 60 $\pm$ 10 ps and 750 $\pm$ 100 ps, which were reduced to 17 $\pm$ 0.2 ps and 200 $\pm$ 22 ps in Z-20. Similar trends were observed for other

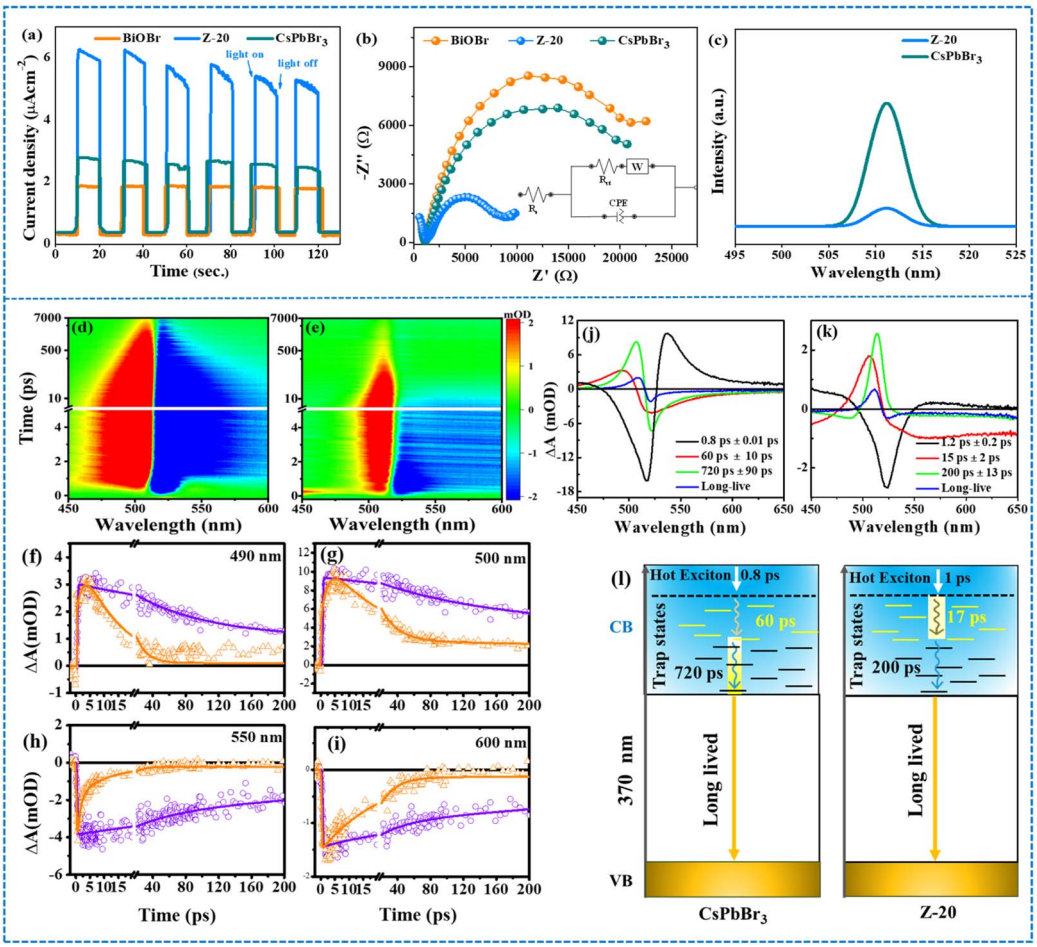

Fig. 5 (a) Photocurrent of BiOBr, $CsPbBr_3$, and heterojunction Z-20 under light/dark conditions. (b) EIS spectra of BiOBr, $CsPbBr_3$ and Z-20. (c) PL spectra of $CsPbBr_3$ and Z-20 at 370 nm excitation wavelength. (d) TA spectra of $CsPbBr_3$, (e) TA spectra of Z-20. (f–i) Kinetic traces for $CsPbBr_3$ (violet) and Z-20 (orange) at probe wavelengths: (f) 490 nm, (g) 500 nm, (h) 550 nm, and (i) 600 nm. The solid lines are fitted lines. (j and k) The decay-associated spectra (DAS) of (j) $CsPbBr_3$ and (k) Z-20. (l) A schematic depiction of the formation and relaxation of charge carriers in $CsPbBr_3$ and Z-20.

wavelengths as well (Fig. 5i and Table S2).[48] The evolution-associated difference spectra (EADS) identified three ultrafast components in $CsPbBr_3$ QDs and Z-20 (Fig. 5j and k).[49] The global analysis revealed lifetimes are 0.8 ± 0.01 ps, 60 ± 10 ps, and 720 ± 90 ps for $CsPbBr_3$ (Fig. 5j) and 1.2 ± 0.2 ps, 15 ± 2 ps, and 200 ± 13 ps for Z-20 (Fig. 5k). Additionally, a long-lived component associated with the charge recombination process was also observed. This is consistent with a nondecaying signal in the TA measurements.

The earlier time-resolved photoluminescence decay investigation of $CsPbBr_3$ has reported recombination lifetimes around 10 ns.[3,50] The faster decay in Z-20 is attributed to the increased rate of depopulation of the involved states through an excited state process. This results in reduced lifetimes in Z-20, indicating the formation of additional trap states in $CsPbBr_3$. Previously, the $CsPbBr_3$–benzoquinone system revealed that the trap state dynamics occurring on the ns–ps time-scale enhanced the catalytic efficiency of the materials.[51,52] The TA measurements were employed to determine the lifetime of exciton formation and relaxation process in $CsPbBr_3$ and Z-20 (Fig. 5l). These lifetimes were used to obtain the corresponding rate constant for the ultrafast processes. The difference in the rate constant between the Z-20 heterojunction and pristine $CsPbBr_3$ was calculated to measure the rate of the formation of trap states in Z-20 (eqn (S1)). The time constant of formation of the trap state decreased from 60 ± 10 ps for $CsPbBr_3$ to 17 ± 0.2 ps for Z-20. The substitution of these lifetimes gives a rate constant of $k_{trap} = 4.2 \times 10^{10}\ s^{-1}$.

The magnitude of the hot electron transfer rate is consistent with the previous studies on the nanostructures.[53–56] The faster rate of formation of the trap state was found in Z-20 compared to pristine $CsPbBr_3$ QDs because of the hot electron transfer in the heterojunction. These photogenerated electrons leave holes in the VB of BiOBr and initiate the interaction of THIQ to generate the iminium radical cation. The hot electrons in CB $CsPbBr_3$ activate $^3O_2$ to form $O_2^{\bullet-}$ and initiate the dehydrogenation reaction.

Photocatalytic semidehydrogenation reaction

Photoredox semidehydrogenation of THIQ was performed in various solvents, including tetrahydrofuran (THF), methanol,

ethanol, acetonitrile, 1,4-dioxane, and dimethylformamide (DMF). Among these, acetonitrile shows the best activity for the semidehydrogenation of THIQ. To elucidate the roles of the photocatalyst, light, and O_2, we performed photoredox reactions with all necessary reaction conditions (see Table S3).

The reactions did not proceed in the absence of photocatalysts or light. The $CsPbBr_3$ QDs showed only a trace amount of conversion of THIQ. In contrast, BiOBr achieved 56% yield for DHIQ in the air atmosphere under visible light. The Z-20 heterojunction achieved full conversion with 97% selectivity for DHIQ (all cases: reported isolated yields) (Fig. S13a and Table S3).

It is important to note that the interaction between substrate molecules and the microstructure of the catalyst surface has been addressed in previous studies. Typically, molecules with a phenyl ring tend to adsorb at particular Lewis acid sites on the catalyst surface.[57] On the surface of BiOBr, Bi^{3+} ions act as Lewis acid sites, due to their vacant 6p orbitals and relatively high electrophilicity to affect the interaction between substrate molecules and the catalyst.[16,57] A previous report confirmed the increased substrate adsorption and affinity at Lewis acid sites through DFT analysis.[58–60]

The time-monitored conversion data with Z-20 showed that the full conversion of THIQ was achieved after 6 hours (Fig. S13b). Interestingly, the extension of the reaction time to 10 hours did not lead to further conversion of DHIQ into IQ (Fig. S13b). The results confirm that the Z-20 heterojunction has a controlled oxidation band potential (VB) suitable for the selective semidehydrogenation of THIQ to DHIQ. The product was characterized by ^{1}H NMR and ^{13}C NMR spectroscopy, and the isolated yield for all cases was reported (Fig. S14a to 16b).

Interestingly, indoline is converted to indole through a $2e^-$ oxidation process. However, 1,2,3,4-tetrahydroquinoline (THQ) was converted to quinoline through $4e^-$ dehydrogenation (Fig. S15a and 16b). The control over the $2e^-$ process by Z-20 is extremely important. In the previous reports with photocatalysis, mostly the $4e^-$ process was followed to form IQ from THIQ (Table S4). A few studies also detected the formation of both THIQ and DHIQ. Only recently, the selective $2e^-$ oxidation of THIQ to DHIQ has been reported by using $Zn_3In_2S_6$, MoS_2/$ZnIn_2S_4$, and $ZnIn_2S_4$ photocatalysts (Table S4).[26,28–30] In this context, this study demonstrates a cheap substitute (Z-20) to the expensive In-based catalysts.

The further oxidation of DHIQ to IQ ($2e^-$ process) was avoided by a suitable choice of photocatalysts in the heterojunction. For the oxidation of DHIQ to IQ, the VBM should be more positive than the THIQ oxidation potential. In this respect, we have designed other heterojunction photocatalysts ($CsPbBr_3$/WO_3) with a more positive VBM (3.06 V *vs.* NHE) of WO_3 than the oxidation potential of THIQ to IQ (2.71 V *vs.* NHE).[29,61] The $CsPbBr_3$/WO_3 heterojunction produced 81% conversion with yields of 24% for DHIQ and 57% for IQ after 10 h (Fig. S17).

Similarly, CdS/BiOBr and TiO_2/BiOBr heterojunctions were designed, producing 74% and 65% yield of DHIQ, respectively.[62,63] The lower yield of DHIQ for these two heterojunctions can be explained by the poor activation of molecular oxygen to $O_2^{\bullet-}$. Therefore, the combination of $CsPbBr_3$ and BiOBr (Z-20) produced the best activity and selectivity for the controlled $2e^-$ semidehydrogenation of THIQ to DHIQ.

Mechanistic study of semidehydrogenation

In Z-20, the photogenerated electrons in the CB activated the adsorbed oxygen on the Pb site of $CsPbBr_3$, to produce $O_2^{\bullet-}$, which was further oxidized to $^1O_2$ in the VB of BiOBr.[17–19] The THIQ interacts with VB holes and produces a cation radical (A) (Fig. 6a).[29,30,64] In addition, $^1O_2$ abstracts hydrogen from the cationic radical to produce an intermediate radical ($I^{\#}$) and hydroperoxide radical ($^{\bullet}$OOH). Interestingly, intermediate $I^{\#}$ was trapped by forming a TEMPO adduct (Fig. S18). Furthermore, $^{\bullet}$OOH reacted with radical $I^{\#}$ to produce product 2 (DHIQ) and hydrogen peroxide (H_2O_2).

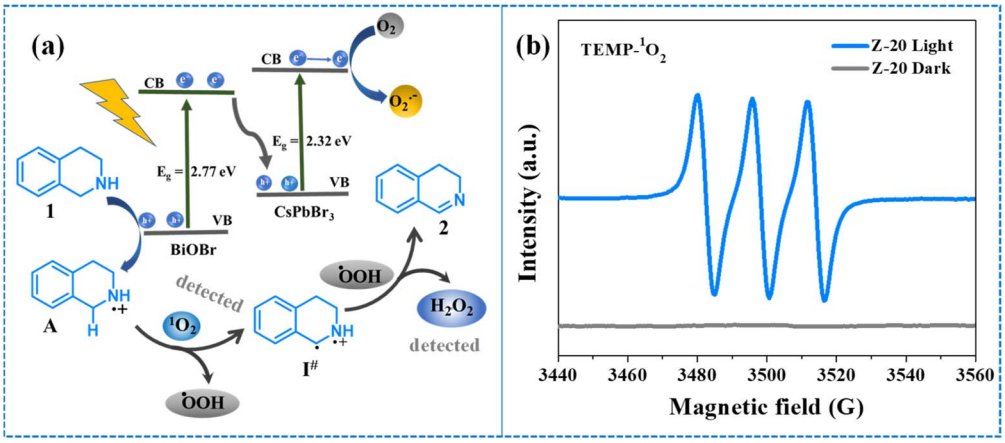

Fig. 6 (a) Proposed mechanism of semidehydrogenation of THIQ. (b) $^1O_2$ radical trapping experiments for the reaction process. Reaction conditions: 10 mg catalyst, 0.5 mmol THIQ, and 3 mL solvent were taken in a borosilicate reaction vial and irradiated with a 15 W blue LED at a temperature of 34 ± 4 °C for 6 hours. The product was isolated by column chromatography on a silica column using varying ratios of ethyl acetate and hexane as the eluent. The product's isolated yield was reported in all cases.

In addition to EPR studies, $O_2^{\bullet-}$ radicals were detected by the *p*-nitro-blue tetrazolium chloride (NBT) test *via* UV-visible absorption spectroscopy (Fig. S19).[65,66] The NBT test confirmed that Z-20 showed a higher amount of $O_2^{\bullet-}$ formation by molecular oxygen activation compared to single catalysts ($CsPbBr_3$ or BiOBr) (Fig. S19). Furthermore, EPR spin-trapping experiments were conducted using TEMP as the trapping agent, confirming the $^1O_2$ formation in the reaction (Fig. 6b).

Additionally, 9,10-diphenylanthracene (DPA) has been used to detect $^1O_2$, with its characteristic UV-vis absorption peaks at 337, 355, 373, and 395 nm (Fig. S20). Upon the generation of $^1O_2$ in the solution, DPA reacts with it, forming an oxidized product and quenching the DPA signals. Consequently, the rate of signal reduction in DPA corresponds to the rate of $^1O_2$ production. The gradual decrease in the intensities of DPA's absorption bands with prolonged irradiation indicates that Z-20 produces $^1O_2$ under light conditions. In addition, $^1O_2$ participated in the photocatalytic semidehydrogenation reaction of THIQs by cooperating with holes (h^+). In this study, we proposed that h^+ is promoted as the driving force for the oxidation of THIQ to generate iminium radical cation, while $^1O_2$ plays a role in hydrogen abstraction to produce H_2O_2.

$^1O_2$ can be generated through two ways: (i) an energy transfer process from $^3O_2$ to $^1O_2$, and (ii) an electron transfer from $O_2^{\bullet-}$ to produce $^1O_2$.[29,67] It is well established that in semiconductors, $O_2^{\bullet-}$ can be converted into $^1O_2$ through the action of holes (h^+) ($O_2^{\bullet-} + h^+ \rightarrow {}^1O_2$).[68,69] To further verify $^1O_2$ production by converting ($O_2^{\bullet-} + h^+ \rightarrow {}^1O_2$), we conducted an additional experiment using a hole scavenger (TEA + DPA + Z-20).[29,70] The rate of $^1O_2$ generation decreased in the presence of the hole scavenger because most of the photogenerated holes were consumed by the scavenger, resulting in a less significant reduction in DPA peak intensity compared to the reaction without a scavenger (Fig. S21).

Similarly, the photocatalytic generation of H_2O_2 is detected through the *o*-tolidine test *via* UV-visible absorption spectroscopy (Fig. S22). The conversion of THIQ and the formation of H_2O_2 directly depend on the photogenerated holes and electron separation for the reduction of $^3O_2$. The *o*-tolidine test also confirmed that Z-20 generated higher concentrations of H_2O_2 compared to individual BiOBr. However, $CsPbBr_3$ did not detect the formation of H_2O_2 due to its insufficient potential of VBM to oxidize THIQ into a radical cation. This confirms that the heterostructure of $CsPbBr_3$ and BiOBr offers a suitable band potential, enhancing charge carrier separation and the semidehydrogenation activity of THIQ, resulting in a higher $^1O_2$ production.

Quenching experiment

Radical quenching experiments were conducted further to elucidate the reaction mechanism (Fig. S23).[29,66,71] Using $AgNO_3$ and triethylamine as electron (e^-) and hole (h^+) scavengers showed a significant decrease in the conversion. This indicates that photogenerated e^- and h^+ play crucial roles in the photocatalytic redox reaction.[72,73] When isopropyl alcohol (IPA) is used as a hydroxyl radical ($^\bullet$OH) scavenger, the photocatalytic performance remains almost unchanged, suggesting that $^\bullet$OH has a negligible effect. Furthermore, *p*-benzoquinone (BQ) and L-histidine were used as $O_2^{\bullet-}$ and $^1O_2$ scavengers, respectively, resulting in the low yields of 22% and 42%. It is confirmed from the quenching experiment that $^1O_2$ is responsible for the dehydrogenation process. As $^1O_2$ is formed by the electron transfer from $O_2^{\bullet-}$, the reaction rate is also influenced by the $^3O_2$ activation process.

It is recognized that $CsPbBr_3$ QDs exhibit poor stability in aqueous media. To address this limitation, we avoided the use of aqueous solvents or formation water during the reaction. The recyclability test demonstrated no significant loss of photocatalytic activity after five cycles in an oxygen atmosphere (Fig. S24).

Furthermore, the UV-visible spectra showed no significant changes in the absorption maxima of Z-20 after photocatalysis (Fig. S25). To verify the stability of the QDs, we performed PXRD, and XPS analyses after the catalytic cycles (Fig. S26). PXRD confirms that there is no change in the phase after the catalysis, whereas a slight broadening of the XPS peaks is observed, indicating partial oxidation of Pb. In contrast, the change in the bandgap of the used catalyst is similar to the fresh one. These findings demonstrate that the $CsPbBr_3$ QDs preserve their crystal structure but with a slight variation in the oxidation state of Pb after catalysis.

Conclusions

In conclusion, the Z-20 heterojunction photocatalyst has been developed for selective DHIQ synthesis through the controlled semidehydrogenation of THIQ under visible light. $CsPbBr_3$ improves the activation of $^3O_2$, and BiOBr modulates the VB potential in Z-20. The formation of the Z-20 heterojunction accelerates the photogenerated charge separation and suppresses the charge recombination process. Ultrafast TA investigation indicates that reaching the trap state in Z-20 originates from $CsPbBr_3$, exhibiting a rate constant of approximately $k_{trap} = 4.2 \times 10^{10}\ s^{-1}$. The faster formation of the trap state enhances photocatalytic activities and initiates the semidehydrogenation reaction. Z-20 achieves the highest yields of DHIQ under atmospheric conditions and visible light.

Author contributions

VK was involved in the synthesis of the catalysts, their characterization, photocatalytic studies, data interpretation, and manuscript writing. VV was involved in product separation (column chromatography) and NMR. DK carried out (photo) electrochemical characterization and data interpretation. SKP and ESSI conducted transient absorption measurements and wrote the corresponding sections. SD and KK carried out EPR and KPFM characterizations and data interpretation. The project design, conceptualization, supervision, data interpretation, manuscript writing, and editing were performed by AI.

Conflicts of interest

There are no conflicts to declare.

Data availability

The detailed data of the above-mentioned manuscript are available in the supplementary information (SI). Supplementary information: experimental details, including synthesis, characterization, spectroscopic and photoelectrochemical measurements, catalytic studies, and ^{1}H NMR, and ^{13}C NMR spectroscopy. See DOI: **https://doi.org/10.1039/d5ta04618a**.

Acknowledgements

AI would like to thank ANRF, India, for the core research grant (Grant No. CRG/2023/002395). VK is thankful to CSIR [09/1217/(0084)/2020-EMR-II] for providing the senior research fellowship.

References

1 H. Huang, D. Verhaeghe, B. Weng, B. Ghosh, H. Zhang, J. Hofkens, J. A. Steele and M. B. J. Roeffaers, *Angew. Chem., Int. Ed.*, 2022, **134**, 202203261.
2 J. Zhou, B. Gao, D. Wu, C. Tian, H. Ran, W. Chen, Q. Huang, W. Zhang, F. Qi, N. Zhang, Y. Pu, J. Qiu, Z. Hu, J. Du, Z. Liu, Y. Leng and X. Tang, *Adv. Funct. Mater.*, 2024, **34**, 2308411.
3 W. Song, K. C. Chong, G. Qi, Y. Xiao, G. Chen, B. Li, Y. Tang, X. Zhang, Y. Yao, Z. Lin, Z. Zou and B. Liu, *J. Am. Chem. Soc.*, 2024, **146**, 3303–3314.
4 E. M. Akinoglu, D. A. Hoogeveen, C. Cao, A. N. Simonov and J. J. Jasieniak, *ACS Nano*, 2021, **15**, 7860–7878.
5 Y. Bai, W. Dong, Q. Zhang, H. She, X. Chen and Q. Wang, *J. Alloys Compd.*, 2025, **1033**, 181237.
6 Y. Fang, Y. Xia, H. She, J. Huang, L. Wang and Q. Wang, *Sep. Purif. Technol.*, 2025, **376**, 134036.
7 Y. Wang and C. Cai, *ACS Catal.*, 2025, **15**, 3451–3463.
8 H. Wang, Z. Chen, Y. Shang, C. Lv, X. Zhang, F. Li, Q. Huang, X. Liu, W. Liu, L. Zhao and L. Ye, *ACS Catal.*, 2024, **14**, 5779–5787.
9 X. Deng, J. Zhang, K. Qi, G. Liang, F. Xu and J. Yu, *Nat. Commun.*, 2024, **15**, 4807.
10 M. Shi, X. Wu, Y. Zhao, R. Li and C. Li, *J. Am. Chem. Soc.*, 2025, **147**, 3641–3649.
11 C. Tang, T. Bao, S. Li, X. Li, H. Rao, P. She and J. S. Qin, *Adv. Funct. Mater.*, 2025, **35**, 2415280.
12 C. Zhang, S. Hu, W. Cui, S. Li, L. Tian, X. Yuan, W. Tariq, K. Yao, K. Zhi, T. Hu and S. Shan, *Chem. Eng. J.*, 2025, **510**, 160317.
13 Y. Zhong, H. Zhu, X. Xie, L. Yang, Y. Shen, Q. Fan, Z. Xie and Z. Le, *Inorg. Chem.*, 2025, **64**, 2706–2715.
14 Z. J. Bai, S. Tian, T. Q. Zeng, L. Chen, B. H. Wang, B. Hu, X. Wang, W. Zhou, J. B. Pan, S. Shen, J. K. Guo, T. L. Xie, Y. J. Li, C. T. Au and S. F. Yin, *ACS Catal.*, 2022, **12**, 15157–15167.
15 H. Cheng, B. Huang and Y. Dai, *Nanoscale*, 2014, **6**, 2009–2026.
16 G. Zhou, B. Lei and F. Dong, *ACS Catal.*, 2024, **14**, 4791–4798.
17 H. Huang, B. Pradhan, J. Hofkens, M. B. J. Roeffaers and J. A. Steele, *ACS Energy Lett.*, 2020, **5**, 1107–1123.
18 Y. Dong, Y. Feng, Z. Li, H. Zhou, H. Lv and G.-Y. Yang, *ACS Catal.*, 2023, **13**, 14346–14355.
19 V. Kumar, S. K. Patel, V. Vyas, D. Kumar, E. S. Subramaniam Iyer and A. Indra, *Chem. Sci.*, 2024, **15**, 13218–13226.
20 X. Zhu, Y. Lin, J. San Martin, Y. Sun, D. Zhu and Y. Yan, *Nat. Commun.*, 2019, **10**, 2843.
21 F. Xu, K. Meng, B. Cheng, S. Wang, J. Xu and J. Yu, *Nat. Commun.*, 2020, **11**, 4613.
22 C. Huang, Y. Huang, C. Liu, Y. Yu and B. Zhang, *Angew. Chem., Int. Ed.*, 2019, **131**, 12142–12145.
23 R. Zhang, N. Chen, T. Ning, Y. Zhang, Y. Ling, X. Wang, W. Zhu and G. Zhu, *Inorg. Chem.*, 2023, **62**, 17433–17443.
24 Z. Zhou, X. Pan, L. Sun, Y. Xie, J. Zheng, L. Li and G. Zhao, *Angew. Chem., Int. Ed.*, 2023, **62**, 202216347.
25 Z. Zhang, W. Liu, Y. Zhang, J. Bai and J. Liu, *ACS Catal.*, 2021, **11**, 313–322.
26 N. O. Balayeva, Z. Mamiyev, R. Dillert, N. Zheng and D. W. Bahnemann, *ACS Catal.*, 2020, **10**, 5542–5553.
27 S. Kato, Y. Saga, M. Kojima, H. Fuse, S. Matsunaga, A. Fukatsu, M. Kondo, S. Masaoka and M. Kanai, *J. Am. Chem. Soc.*, 2017, **139**, 2204–2207.
28 M. Zheng, J. Shi, T. Yuan and X. Wang, *Angew. Chem., Int. Ed.*, 2018, **57**, 5487–5491.
29 J. Luo, X. Wei, Y. Qiao, C. Wu, L. Li, L. Chen and J. Shi, *Adv. Mater.*, 2023, **35**, 2210110.
30 M. Hao, X. Deng, L. Xu and Z. Li, *Appl. Catal., B*, 2019, **252**, 18–23.
31 H. Jiang, M. Liu, X. Lian, M. Zhu and F. Zhang, *Angew. Chem., Int. Ed.*, 2024, **63**, 202318850.
32 Z. Zhang, L. Li, Y. Jiang and J. Xu, *Inorg. Chem.*, 2022, **61**, 3351–3360.
33 L. Wang, B. Cheng, L. Zhang and J. Yu, *Small*, 2021, **17**, 2103447.
34 S. Lin, Z. Sun, X. Qiu, H. Li, P. Ren, H. Xie and L. Guo, *Small*, 2024, **20**, 2306983.
35 Z. H. Zhao, H. Wang, J. Li, X. Qiao, Z. Liu, Z. Ren, M. Yuan and J. Zhang, *J. Am. Chem. Soc.*, 2024, **146**, 29441–29449.
36 B. Rawat, V. R. Battula, P. K. Nayak, D. Ghosh and K. Kailasam, *ACS Appl. Mater. Interfaces*, 2023, **15**, 53604–53613.
37 M. Banoo, R. S. Roy, M. Bhakar, J. Kaur, A. Jaiswal, G. Sheet and U. K. Gautam, *Nano Lett.*, 2022, **22**, 8867–8874.
38 L. Li, X. Dai, K. Gao, H. Yu, F. Chen, W. Wang, J. Ning and Y. Hu, *Chem. Eng. J.*, 2025, **514**, 163193.
39 L. Li, C. Guo, T. Li, C. Yang, F. Chen, W. Wang, R. Yan, J. Ning and Y. Hu, *Appl. Surf. Sci.*, 2024, **651**, 159220.
40 C. Wang, Y. Zhao, C. Cheng, Q. Li, C. Guo and Y. Hu, *Coord. Chem. Rev.*, 2024, **521**, 216177.
41 Y. Jiang, H. Y. Chen, J. Y. Li, J. F. Liao, H. H. Zhang, X. D. Wang and D. B. Kuang, *Adv. Funct. Mater.*, 2020, **30**, 2004293.

42 X. D. Wang, Y. H. Huang, J. F. Liao, Y. Jiang, L. Zhou, X. Y. Zhang, H. Y. Chen and D. B. Kuang, *J. Am. Chem. Soc.*, 2019, **141**, 13434–13441.
43 L. Lin, Y. Ma, J. J. M. Vequizo, M. Nakabayashi, C. Gu, X. Tao, H. Yoshida, Y. Pihosh, Y. Nishina, A. Yamakata, N. Shibata, T. Hisatomi, T. Takata and K. Domen, *Nat. Commun.*, 2024, **15**, 397.
44 Y. Zheng, Y. Chen, B. Gao, B. Lin and X. Wang, *Adv. Funct. Mater.*, 2020, **30**, 2002021.
45 H. Wang, W. Lu, P. Xu, J. Luo, K. Yao, J. Zhang, X. Wei, S. Peng, H. Cheng, H. Hu and K. Sun, *ACS Sustain. Chem. Eng.*, 2023, **11**, 5963–5972.
46 J. S. Manser, J. A. Christians and P. V. Kamat, *Chem. Rev.*, 2016, **116**, 12956–13008.
47 T. Wang, H. Liu, X. Wang, L. Tang, J. Zhou, X. Song, L. Lv, W. Chen, Y. Chen and X. Li, *ACS Catal.*, 2023, **13**, 13902–13911.
48 S. Bera, A. Tripathi, T. Titus, N. M. Sethi, R. Das, N. Afreen, K. V. Adarsh, K. G. Thomas and N. Pradhan, *J. Am. Chem. Soc.*, 2024, **146**, 20300–20311.
49 I. H. M. Van Stokkum, D. S. Larsen and R. Van Grondelle, *Biochim. Biophys. Acta, Bioenerg.*, 2004, **1657**, 82–104.
50 N. Mondal and A. Samanta, *Nanoscale*, 2017, **9**, 1878–1885.
51 K. Wu, G. Liang, Q. Shang, Y. Ren, D. Kong and T. Lian, *J. Am. Chem. Soc.*, 2015, **137**, 12792–12795.
52 C. Harris and P. V. Kamat, *ACS Nano*, 2010, **4**, 7321–7330.
53 T. Okuhata, T. Katayama and N. Tamai, *J. Phys. Chem. C*, 2020, **124**, 1099–1107.
54 Y. Liu, Q. Chen, Q. Chen, D. A. Cullen, Z. Xie and T. Lian, *Nano Lett.*, 2020, **20**, 4322–4329.
55 K. Wu, H. Zhu, Z. Liu, W. Rodr and T. Lian, *J. Am. Chem. Soc.*, 2012, 10337–10340.
56 M. Li, S. K. Cushing, Q. Wang, X. Shi, L. A. Hornak, Z. Hong and N. Wu, *J. Phys. Chem. Lett.*, 2011, **2**, 2125–2129.
57 J. Lee, A. Kumar and H. Tüysüz, *Angew. Chem., Int. Ed.*, 2024, **63**, 202404496.
58 J. Sheng, Y. He, M. Huang, C. Yuan, S. Wang and F. Dong, *ACS Catal.*, 2022, **12**, 2915–2926.
59 J. Jiang, K. Zhao, X. Xiao and L. Zhang, *J. Am. Chem. Soc.*, 2012, **134**, 4473–4476.
60 X. Cao, A. Huang, C. Liang, H. C. Chen, T. Han, R. Lin, Q. Peng, Z. Zhuang, R. Shen, H. M. Chen and Y. Yu, *J. Am. Chem. Soc.*, 2022, **144**, 3386–3397.
61 A. Singha, J. Kaishyop, T. S. Khan and B. Chowdhury, *ACS Appl. Nano Mater.*, 2023, **6**, 21818–21828.
62 A. K. Singh, A. Jaryal, S. K. Patel, D. Kumar, E. S. Subramaniam Iyer, K. Kailasam and A. Indra, *J. Mater. Chem. A*, 2023, **11**, 16724–16733.
63 J. Qiu, P. Zhang, M. Ling, S. Li, P. Liu, H. Zhao and S. Zhang, *ACS Appl. Mater. Interfaces*, 2012, **4**, 3636–3642.
64 X. Y. Lin, M. Y. Qi, Z. R. Tang and Y. J. Xu, *Appl. Catal., B*, 2022, **317**, 121708.
65 V. Kumar, V. Vyas, D. Kumar, A. K. Kushwaha and A. Indra, *Chem. Sci.*, 2024, **15**, 15448–15455.
66 Y. Deng, W. Liu, R. Xu, R. Gao, N. Huang, Y. Zheng, Y. Huang, H. Li, X. Y. Kong and L. Ye, *Angew. Chem., Int. Ed.*, 2024, **63**, 202319216.
67 Y. Nosaka and A. Y. Nosaka, *Chem. Rev.*, 2017, **117**, 11302–11336.
68 S. Jin, W. Shao, X. Luo, H. Wang, X. Sun, X. He, X. Zhang and Y. Xie, *Adv. Mater.*, 2022, **34**, 2206516.
69 J. Qiu, H. Zhai, Y. Zhao, Y. Jin, Z. Li, H. Wang, Z. Li, J. Wang and J. B. Baek, *Angew. Chem., Int. Ed.*, 2025, **137**, 202508078.
70 A. Augustin, P. Ganguly, S. Shenoy, C. Chuaicham, S. C. Pillai, K. Sasaki, A. F. Lee and K. Sekar, *Adv. Sustainable Syst.*, 2024, 2400321.
71 F. Puga, J. A. Navío and M. C. Hidalgo, *Appl. Catal., A*, 2024, **685**, 119879.
72 A. Indra, R. Beltrán-Suito, M. Müller, R. P. Sivasankaran, M. Schwarze, A. Acharjya, B. Pradhan, J. Hofkens, A. Brückner, A. Thomas, P. W. Menezes and M. Driess, *ChemSusChem*, 2021, **14**, 306–312.
73 Y. Wang, R. Godin, J. R. Durrant and J. Tang, *Angew. Chem., Int. Ed.*, 2021, **60**, 20811–20816.